PAPER • OPEN ACCESS

Nitrogen infusion R&D at DESY a case study on cavity cut-outs

Nitrogen infusion R&D at DESY a case study on cavity cut-outs

Marc Wenskat[1,2] (ID)**, Christopher Bate**[1,2]**, Arti Dangwal Pandey**[2]**, Arno Jeromin**[2]**,
Thomas F Keller**[1,2] (ID)**, Jens Knobloch**[3,4]**, Julia Köszegi**[3,5]**, Felix Kramer**[3,4]**, Oliver Kugeler**[3]**,
Satish Kulkarni**[2]**, Detlef Reschke**[2]**, Jörn Schaffran**[2]**, Guilherme Dalla Lana Semione**[1,2]**,
Sven Sievers**[2]**, Lea Steder**[2] (ID)**, Andreas Stierle**[1,2]** and Nicholas Walker**[2]

[1] Physics Department, Universität Hamburg, Luruper Chaussee 149, 22761 Hamburg, Germany
[2] Deutsches Elektronen-Synchrotron, Notkestrasse 85, 22607 Hamburg, Germany
[3] Helmholtz-Zentrum Berlin, Albert-Einstein-Straße 15, 12489 Berlin, Germany
[4] Department of Physics, Universität Siegen, Walter-Flex-Str. 3, 57068 Siegen, Germany
[5] Department of High-Frequency and Semiconductor System Technologies, Technische Universität
Berlin, Gustav-Meyer-Allee 25, 13355 Berlin, Germany

E-mail: marc.wenskat@desy.de

Abstract

A first series of nitrogen infusion runs of 1.3 GHz single-cell cavities at DESY resulted in an
unexpected and severe deterioration observed during the vertical cold test. To investigate the
origin of the deterioration, one of the cavities underwent extensive radio-frequency
measurements and a temperature- and magnetic field-mapping was performed in collaboration
with the Helmholtz-Zentrum Berlin. After combining all results, regions of interests were
identified and cut-out of the cavity. Subsequent surface analysis techniques (EBSD, PALS,
PIXE, SEM/EDX, SIMS, XPS) were applied in order to identify the microscopic origin of the
deterioration and especially the differences between hot and cold spots as well as quench spots.
An excess of niobium carbides, reducing the thermal conductivity, was identified as the
probable cause for the deterioration, and the size- and density-distributions were observed to be
crucial for the resulting performance reduction. The origin for the local differences in the
niobium carbide formation between hot and cold spots is an effect of preexisting variations of
the crystal structure.

Keywords: superconducting cavities, niobium, nitrogen infusion, niobiumcarbides

(Some figures may appear in colour only in the online journal)

1. Motivation

The European x-ray free-electron laser (XFEL) continuous-
wave upgrade requires superconducting radio-frequency (rf)
cavities with reduced surface resistance (high Q_0-values)
for increased duty cycles at 2 K and medium accelerat-
ing gradients while maintaining high accelerating gradients
for short-pulse operation [1, 2]. Since cavities after a so-
called *nitrogen infusion* exhibit improvements matching these
requirements [3, 4], DESY started a research project to adapt
the infusion process for European XFEL cavities. The over-
all aim of the DESY approach is to establish a stable, repro-
ducible recipe and to identify all key parameters for the pro-
cess and the niobium surface evolution which is crucial for the
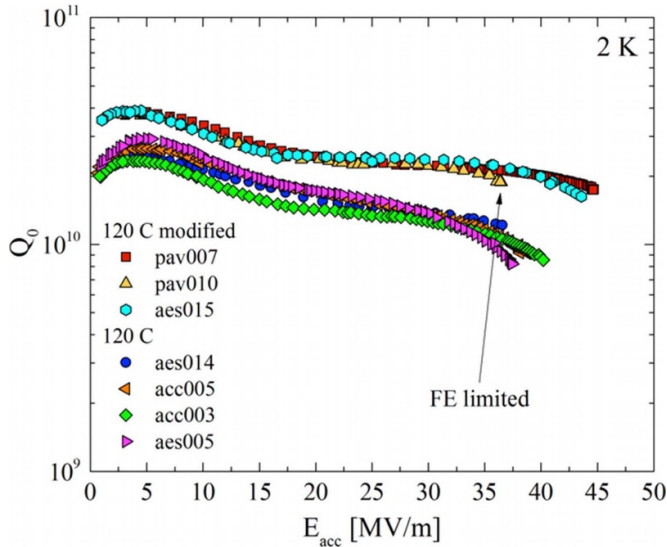improvement.

Figure 1. Quality factor Q_0 versus accelerating field E_{acc} curves measured at 2 K which show the effect of nitrogen infusion at 120 °C versus the standard treatment. Image taken from [3] published under CC BY.

2. Infusion process

Introducing nitrogen as interstitial into the near-surface niobium lattice to further improve the rf performance of the cavity has been discovered at the Fermi National Accelerator Laboratory (FNAL) [3, 5] and further studied at various other laboratories [4, 6–9]. In this section, an overview of the observed cavity improvement and the infusion recipe is presented in the following paragraph.

2.1. RF performance

Nitrogen infused cavities have been shown to have an improved quality factor Q_0 over the whole accelerating field range compared to conventional treated cavities as shown in figure 1. At the same time, the maximum achievable accelerating field seems to increase under certain circumstances [3], although this is not the case for all applied temperatures [4]. The underlying physical effect causing the improvement is not fully understood, although various experiments showed that nitrogen as an agent is crucial [3, 4, 6, 10–13].

2.2. Infusion recipe

The nitrogen infusion recipe, as described by FNAL [3], starts with a heat treatment of 800 °C for 3 h in a pressure below 5×10^{-6} mbar, see figure 2. The step is deemed to be necessary to remove the passivating natural surface oxides, namely Nb_2O_5, NbO_2 and NbO, and creates a reactive niobium surface. While still in vacuum, the cavity is cooled down to 120 °C and nitrogen is continuously injected at a partial pressure of 0.03 mbar which is actively maintained by pumping and the cleanliness of the nitrogen has to be 6.0 or better. This state is maintained for 48 h. In this phase, nitrogen enters the material as an interstitial and does not form niobium nitrides,
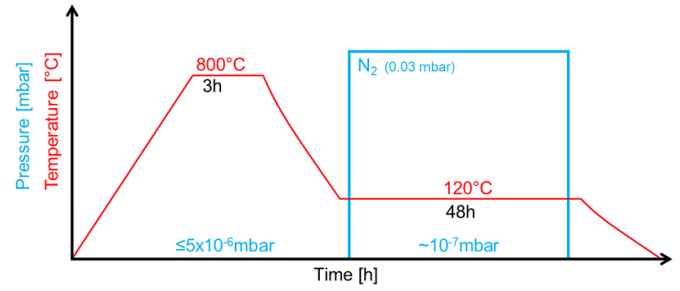

Figure 2. Schematic of the infusion recipe.

as for the doping recipe [14], since the cavity temperature is below the nitride formation temperature. After 48 h, the furnace is evacuated again and the cavity is cooled down to room temperature. The temperature during the 48 h has been varied to study its influence and recipes with up to 180 °C exist, which show a more 'doping-like' behavior [3, 4]. An additional point is the installation of so-called *niobium caps* onto the cavity beam pipes before the treatment - see figure 3. Initially, they were installed to prevent a titanium contamination in the FNAL furnace from entering the cavity [15]. How these caps affect the inner atmosphere during this procedure, e.g. act as a filter or getter material or if they are necessary at all has not yet been clarified. Results from other labs [4, 8] showed that modifications of the FNAL recipe were necessary to transfer it to a specific furnace system in order to be successful while some changes were rather accidentally discovered. It is therefore quite likely that at the current point neither the optimal settings for the controlled process parameters nor all relevant critical parameters are identified.

3. Infusion R&D at DESY

Since there is currently no universal infusion recipe, we started an independent research project to establish an infusion process specifically for the DESY facilities. A series of single-cell cavities were prepared using the standard XFEL recipe and underwent baseline tests before any infusion treatment. For each run, a series of fine-grain niobium samples from high residual resistance ratio (RRR) European XFEL niobium sheets were prepared and placed into the furnace together with the cavities. In this section, the furnace used for these studies, the first single-cell cavities and their results and the sample results from these runs will be introduced.

3.1. DESY furnace

The furnace was successfully used during the preparation of the European XFEL cavity production, mostly for the 800 °C bake, necessary for the outgassing of hydrogen from the niobium and release mechanical stress [16, 17]. The process vacuum pressure for the outgassing at 800 °C has to be below 1×10^{-5} mbar. The cavity preparation work flow foresees a final chemical treatment to remove any possible contamination after the 800 °C bake. Those two facts result in less stringent vacuum requirements regarding cleanliness and partial
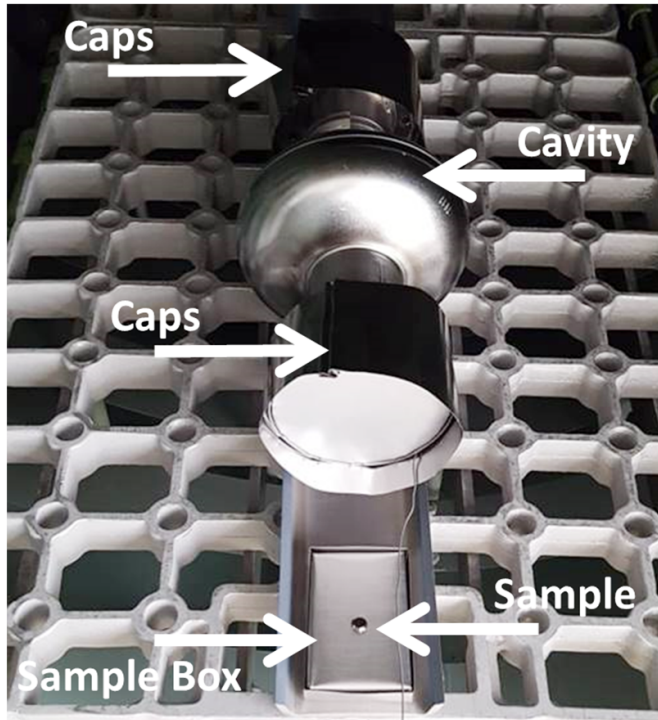
Figure 3. A single-cell cavity installed in the furnace. Samples were placed inside a niobium box to simulate the interior of a cavity. The niobium caps cover the flanges of the cavity.

pressures. Therefore it was unclear whether the furnace could achieve the values specified in the infusion recipe by FNAL. Given the experience at other labs, it was also unclear if these values are actually necessary.

The furnace has a total volume of 7 m^3 with an effective heating zone of $1800 \times 625 \times 660$ mm^3 and was produced by the company *Ipsen International GmbH*. The maximum achievable, stable temperature is $T_{max} = 1100°C$ and the furnace has a temperature stability of $\pm 2°C$. The door of the furnace is double sealed by EPDM O-rings with a vacuum in between. Other accessories such as pumps, gauges etc are sealed by standard EPDM seals. The pre-pumps are rotary vane pumps and a roots pump. The main pumps are two Varian turbo-molecular pumps (TMP), each with a total pumping speed of 6000 l s^{-1}. The pressure during the baking is monitored with an ionization gauge IKR050 by Pfeiffer Vacuum which is sensitive between 2×10^{-9} mbar and 5×10^{-3} mbar, and with a Pirani gauge during the infusion process. More recently, an additional full-range gauge has been installed on the opposite side of the furnace to control the pressure homogeneity in the recipient. Residual Gas Analysis (RGA) are taken continuously except during the nitrogen injection at 120 °C.

3.2. Cavity studies

All studies were carried out on 1.3 GHz single-cell cavities made of two long TESLA-type end-groups and a geometry factor of 271.5 Ω [18]. The material was fine-grain niobium with a RRR above 300.

3.2.1. Cavity preparation. The three cavities presented here were last tested in 2006/2007 and have been since stored in double-sealed clean room bags and with plastic caps. The first single-cell cavity which underwent the infusion treatment, 1DE18, received an additional mild hydrogen fluoride (HF) acid treatment, prior to the reference test, since a small fraction of the inner surface of one beam pipe was oxidized after the long-term storage. The cavities underwent a reference test at 2 K before any further treatment was done and no change in the performance compared to the test before storage was found. The cavities showed a typically good performance for the standard recipe, see the reference tests in figure 4, and were then prepared for the infusion procedure. The preparation includes the disassembly of all antenna and vacuum components, a high-pressure rinsing of the inner surface to remove any particle contamination from the disassembly, and the installation of the niobium caps onto the flanges. The niobium caps underwent a chemical polishing of $\approx 10 \mu m$ before each use. After preparation, the cavity was sealed in a clean-room foil bag and transported to the furnace. The bag was opened and the cavity installed into the furnace, together with samples described in section 3.3, under local clean-room conditions as shown in figure 3.

3.2.2. Infusion runs and cavity tests. The infusion parameters of all three cavities are given in table 1.

1DE18. During the nitrogen infusion, the nitrogen pressure was three orders of magnitude lower than specified in the FNAL recipe during the 120 °C bake. Due to the high throughput of the turbo molecular pump on the opposite side of the injection, and the location of the gauge used to regulate the mass, which was too close to the injection valve. This caused a pressure gradient across the furnace and the low pressure at the cavity. In addition, the pressure at 800 °C was a magnitude higher than the specified value and the temperature was held for only 2 h. The result of the cavity test after the treatment and the reference test is shown in figure 4. Q_0 versus T measurements before and after the treatment showed an increased residual resistance from 3.8 nΩ to 35 nΩ and a decrease of the reduced gap value $\Delta/k_B T_c$ from 1.97 to 1.79.

1DE17. After the deterioration of the performance of 1DE18, the same temperature cycle but without a nitrogen injection during the 120 °C baking was performed for the single-cell cavity 1DE17. The goal was to exclude the nitrogen injection itself as the source of the deterioration, and to check the cleanliness of the oven, already in doubt due to the observation of precipitates on samples placed in the furnace during the 1DE18 treatment. It was decided to use the pre-pumps during the nitrogen injection, since during the previous treatment, the pumping speed of TMP was to high and the pressure close to their operational limits.

The performance of the second single-cell cavity 1DE17 after the treatment showed similar behavior to 1DE18 (see figure 4). Hence, the nitrogen injection and any possible contamination of the injection process was excluded as the origin for
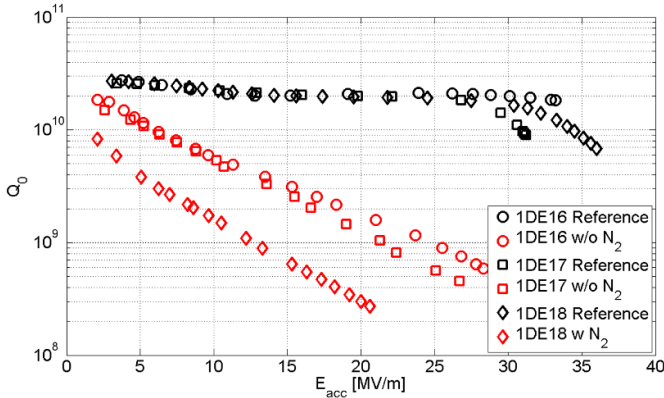
Figure 4. Quality factor Q_0 versus accelerating field E_{acc} of the three single-cell cavities taken at 2 k. Reference measurements are black, measurements after the treatments are in red. 1DE18 (diamonds), 1DE17 (squares) and 1DE16 (circles) showed the same deterioration, regardless of the injection of nitrogen into the furnace. The cavities after the infusion were not limited by quench but simply by power available.

Figure 5. Quality factor Q_0 versus accelerating field E_{acc} at 2 K for 1DE16. The reference measurement (black diamonds) had no field emission (FE) and was quench limited. After the first infusion run without nitrogen at 120 °C the cavity showed a reduced quench field (blue squares). After the second infusion run without nitrogen at 120 °C a strong deterioration and no field emission (FE) or quench was observed (red circles).

the deterioration, and brought the furnace pressure or a contamination of the furnace itself in focus.

1DE16. Prior to the treatment of the third cavity 1DE16, a bake-out cycle (1100 °C for 4 h) of the furnace and an extensive leak search was done to improve the total and partial pressures. 1DE16 underwent the same temperature cycle without nitrogen injection as 1DE17. The first 'infusion run without nitrogen' of 1DE16 resulted in a different kind of deterioration. Although the quench field dropped by 6 MV m^{-1} and the quench spot also shifted its position (see details in section 4.1), the quality factor and the residual resistance of $3.5 \pm 0.3\,n\Omega$ remained at the level before the treatment, as shown in figure 5. The decision was made to treat the cavity a second time with identical parameters. Afterward, the performance of 1DE16 was similar to the deteriorated performance of 1DE17 and 1DE18 post-treatment, see figure 4 and 5.

Discussion. Some evidence suggest that the actual step at which the deterioration is caused is the 800 °C part of the infusion process. (i) The pressure at 800 °C improved for each run of the three cavities, see table 1. At the same time, although the slope of the quality factor Q_0 was similar for each cavity (for 1DE16 only after the 2nd run), the absolute value of the quality factor Q_0 improved with each cavity, hinting that a better pressure at 800 °C results in a less severe deterioration. A detailed analysis of the RGAs obtained 30 min after achieving 800 °C during these runs showed rather large contributions from carbon monoxide and carbon dioxide, see figure 6. The background pressure during the 120 °C phase of the different runs was always on the order of 4×10^{-7} mbar.

(ii) The same precipitates which were observed on samples after the infusion runs (see section 3.3) were observed on a sample installed during one standard European XFEL 800 °C bake of a different, unrelated cavity, using the same furnace.
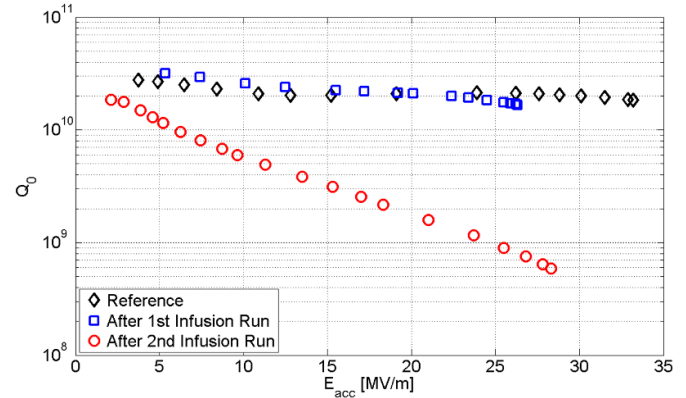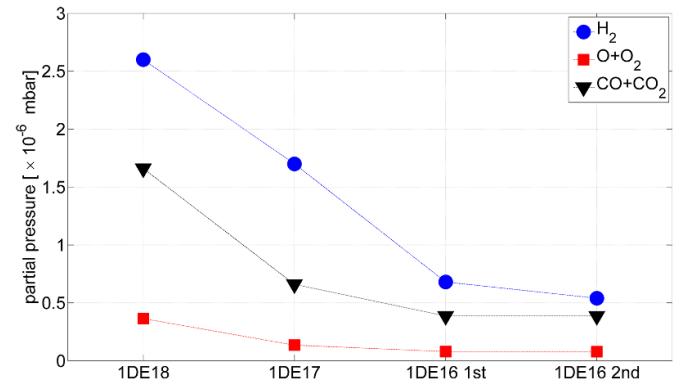

Figure 6. Partial pressure for the masses 2 (H_2), 16 + 32 (O + O_2) and 28 + 44 (CO/N_2 + CO_2) for the different runs after 30 min of the 800 °C phase.
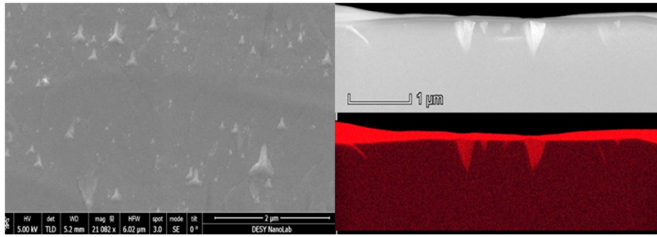
3.3. Sample studies

3.3.1. Sample preparation. The samples were made of niobium sheets from the European XFEL cavity production. Sheets from three different vendors which were still available after the cavity production were cut in a series of standardized sample shapes. The samples underwent the standard European XFEL cavity preparation, including electrochemical surface removal of ≈ 120 to $140\,\mu$m, a first outgassing bake at 800 °C for 3 h, a second chemical polishing of $\approx 30\,\mu$m and another bake of 120 °C for 48 h while undergoing ultra-sonic bath and high-pressure rinsing in a clean-room environment in between the steps to assure particle- and grease-free surfaces. This recipe has been developed over several years, see e.g. [16, 17] for details. The samples were then placed within a niobium box made from cavity-grade material to simulate the interior of the cavity, see figure 3.
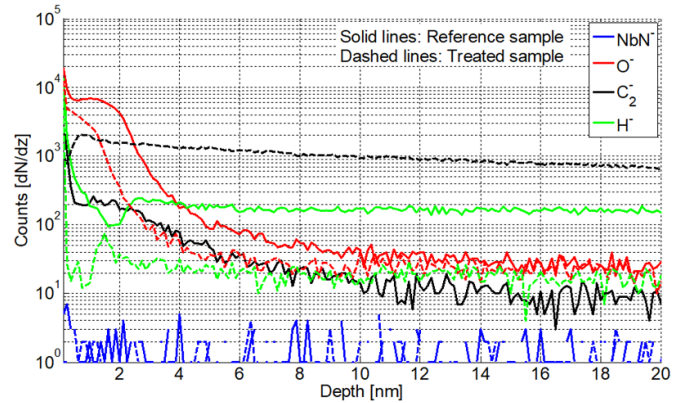
3.3.2. Observations. On all samples, star-like precipitates were observed, see figure 7. These structures are optically

Table 1. RF results and key bake parameters of the first three cavities.

	1DE18	1DE17	1DE16 1st run	2nd run
Material	Ningxia fine grain	Ningxia fine grain	Plansee fine grain	
Reference @ 2 K				
$E_{acc,max}[\frac{MV}{m}]$	37.7 - BD	31.2 - BD	32.2 - BD	
$Q_0(4\,MV\,m^{-1})$ $[\times 10^{10}]$	2.8	2.5	2.7	
Baking Parameters				
p_{max} @ 800 °C $\times 10^{-6}$ [mbar]	20	11	5.7	6.0
p_{N_2} @ 120 °C [mbar]	$7 - 300$ $\times 10^{-5}$	w/o	w/o	w/o
RF Test @ 2 K				
$E_{acc,max}[\frac{MV}{m}]$	20.2 no FE	19.5 no FE	26.3 - BD no FE	28.3 no FE
$Q_0(4\,MV\,m^{-1})$ $[\times 10^{10}]$	0.5	1.2	3.2	1.3

Figure 7. SEM of a sample surface (left) and a bright field transmission electron microscopy (TEM) and TEM-EDX of a lamella from the same sample (top- and bottom-right). The element shown in the bottom-right is carbon. Star-shaped carbon-enriched precipitates protruding from the surface are observed.

Figure 8. ToF-SIMS data of two samples, counts per second vs. depth are shown. The samples are from the same niobium sheet and were treated identically, except one was infused together with a single-cell cavity. The solid lines are the values for the reference sample, the dashed for the infusion run sample.

identical to the already identified β-Nb$_2$N structures, which are common for nitrogen doped cavities [14]. However the energy-dispersive x-ray (EDX) spectrum of the precipitates on our samples clearly showed that they do not contain any nitrogen but are carbon-enriched. Subsequent TEM analysis utilizing electron diffraction identified the precipitates as Nb$_2$C. In addition, time-of-flight secondary-ion mass spectrometry (ToF-SIMS) measurements indicated that samples baked in the furnace together with cavities had a significant increase of interstitial carbon but an absence of nitrogen [2], see figure 8. Further treatments of these samples, e.g. an HF rinsing, did not remove the star-like structures. In agreement to that, two of the treated cavities (namely 1DE18 and 1DE17) underwent an HF rinsing and were retested. Assuming that no additional contamination except the star-like structures is the cause of the performance deterioration and using the sample results, no change was expected and indeed none was observed. The reaction kinetics of Nb$_2$C indicate that the precipitate growth below 800 °C is strongly suppressed [19, 20], strengthening further the assumption that this phase of the bake is the cause of the deterioration.

Following infusion runs on cavities (not presented here) revealed a more complex situation [21]: samples outside the niobium box did not form niobium carbides compared with samples within the box for the same infusion run. For bake cycles resulting in cavity performance with either no or less severe degradation, samples inside the niobium box still showed niobium carbide precipitates. Therefore it was decided to make cut-outs from 1DE16 to test the hypothesis that niobium carbide precipitates where forming on the inner surface of the cavity.

4. RF characterization of 1DE16

Cavity 1DE16 was chosen to be cut and a thorough study of the cavity was done prior to the dissection in order to identify all regions of interest. To that end, data taken at DESY was combined with a temperature- and magnetic-field map (T- and
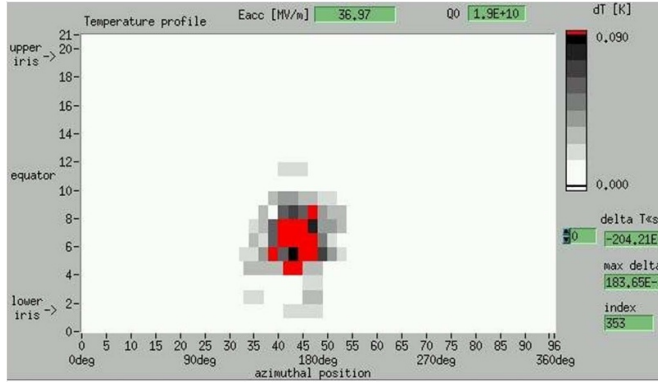
Figure 9. Temperature-map of 1DE16 from before storage. A clear heating at $\approx 170\%$ below the equator is observed. No thermal heating prior the quench field was observed. The second sound measurement in the recent reference test detected the same spot as quench location.

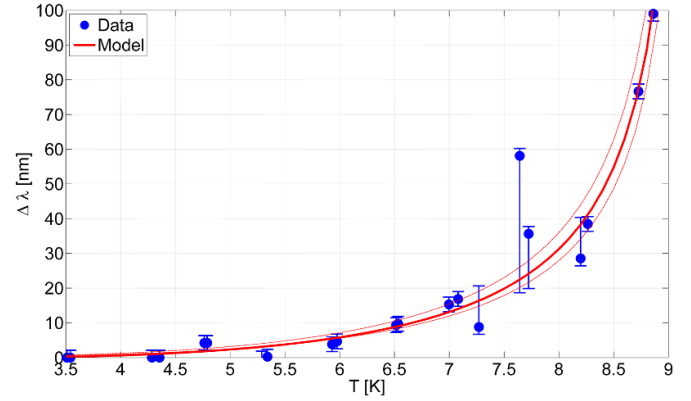**Figure 10.** Change of the penetration depth as a function of the cavity temperature. The outliers at $\approx 7.6k$ are due to helium pressure variations during the measurement and the best fit is obtained with a $\ell = 14 \pm 8$ nm. The bars give the 95% confidence level.

H-map) of the cavity, which was taken in a collaboration with Helmholtz-Zentrum Berlin (HZB), and is presented in this section.

4.1. Measurements at DESY

4.1.1. Quench spot detection. The rf performance of 1DE16 remained unchanged after storage of about 10 years on shelf. The T-map taken at DESY before storage revealed a quench spot at about $170°$ below the cavity equator [22], see figure 9. No thermal heating prior to the quench field was observed, hence a magnetic effect was assumed to be the dominating origin. After the storage and an additional HPR during cavity assembly, the same spot at the same quench field level was detected with the second sound system at DESY [23, 24]. The quench field after the first infusion run decreased from (32.2 ± 0.9) MV m^{-1} to (26.3 ± 0.7) MV m^{-1}, see figure 5. The quench spot itself changed its position as well. The most likely quench spot was found to be at $70 \pm 10°$ using the second system, if it is assumed that the quench took place at the equator region. It has to be noted that the cavity did not quench after the second infusion run but was limited by available rf power and the maximal accelerating field increased slightly to (28.3 ± 0.8) MV m^{-1}.

4.1.2. Frequency vs. temperature measurement. In addition, the resonance frequency versus temperature was measured to determine the mean free path in the rf layer after the second infusion run. The Slater theorem relates a shift in the frequency of the cavity to a change of its resonating volume if the pressure of the helium bath remains constant [25]. The frequency shift can be translated into a change of the penetration depth according to

$$\Delta \lambda = \frac{G}{\pi \mu_0 f^2} \Delta f \qquad (1)$$

with G being the geometry constant of the cavity, f as the frequency and Δf as the frequency change. Having obtained the

penetration depth shift $\Delta \lambda$, one can use the Casimir-Gorter relation [26] to obtain λ_0, which is the penetration depth at 0 k:

$$\Delta \lambda = \lambda(T) - \lambda_0 = \frac{\lambda_0}{\sqrt{(1 - (T/T_c)^4)}} - \lambda_0 \qquad (2)$$

with T_c as the critical temperature of the superconductor. In the Pippard-limit, λ_0 is directly related to the mean free path ℓ of the cavity via [27]

$$\lambda_0 = \lambda_L \sqrt{1 + \frac{\pi \xi_0}{2\ell}}. \qquad (3)$$

Values for the London penetration depth λ_L (32 nm) and coherence length of the Cooper pairs ξ_0 (39 nm) for niobium are taken from literature [28]. The measured $\Delta \lambda$ vs. temperature curve is shown in figure 10. The best fit of the curve is obtained with a value for the mean free path of $\ell = 14 \pm 8$ nm and a $T_c = 9.3 \pm 0.3 k$. The value of the mean free path is smaller than half the coherence length ξ_0 which shows that the material is in the dirty limit. Using the relation [29]

$$\ell[\text{nm}] = 2.7 \cdot \chi \qquad (4)$$

with χ as the value of the RRR, the RRR of the material can be estimated to be 5 ± 3. Since the temperature range of this analysis is up to T_c, the probed layer has a thickness of up to 160 nm. Such low mean free path value shows that the cavity was loaded with a significant amount of interstitials during the infusion run which diffused deep into the material.

4.2. Measurements at HZB

The HZB developed a temperature- and magnetic-field-mapping system which can be applied to single-cells during the rf tests with a three-dimensional control over the ambient magnetic field using three sets of Helmholtz-coils [30]. Several measurements of 1DE16 with this set up installed were done.
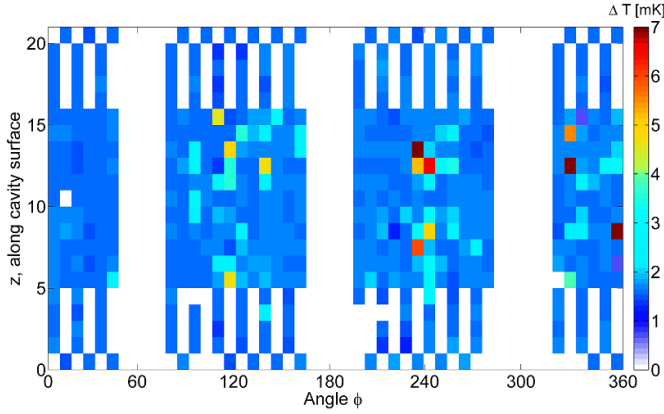
Figure 11. Temperature map of 1DE16 taken at 14 MV m^{-1} and 1.8 K- position along the cavity surface (Δ z $\approx$ 8.9 mm) vs. rotational angle ($\Delta\phi = 7.3°$ or $\approx$ 13.2 mm at the equator). White areas are the position of the H-Map cards. An average temperature increase of $\Delta T = 1.6 \pm 0.1 mK$ is observed.

4.2.1. Temperature mapping. The result of the T-map measurement at 1.8 K is shown in figure 11. The measurements show that the average temperature increase at 14 MV m^{-1} and at 1.8 K is 1.6 ± 0.1 mK while some localized spots with an temperature increase higher than average are observed.

4.2.2. Sensitivity to trapped flux. The surface resistance R_s of a cavity can be written as the sum of three contributions: (i) a temperature and frequency dependent part R_{BCS}, (ii) an intrinsic residual resistance R_0 arising from lattice properties and (iii) a trapped flux resistance R_{fl}. The trapped flux resistance R_{fl} can be calculated via $\eta \cdot S \cdot B_{ext}$ with η being the efficiency to trap flux during cooldown, S as the sensitivity to trapped flux of the material and B_{ext} the external applied magnetic field. While η is a property of the bulk material, S is a property of the near-surface layer which is strongly influenced by applied treatments [31, 32]. Hence, obtaining an estimate for S will possibly help to identify and understand the underlying deterioration process. Applying the same cooldown procedure to a cavity multiple times, resulting in the same η, and varying the external applied magnetic field B_{ext} while crossing T_c, an estimate of the trapped flux contribution and the sensitivity to trapped flux S can be derived. To quantify the contribution to the rf losses from the flux trapped during cooldown, the surface resistance R_s versus accelerating field E_{acc} measurements at 16 mbar (1.8 k) for two different external applied magnetic fields B_{ext}, shown in figure 12, were measured. The difference in the surface resistance between these two measurements is $(4.3 \pm 0.2)n\Omega$ below 9 MV m^{-1} and increases continuously up to $(8.8 \pm 0.4)n\Omega$ at 14 MV m^{-1}. From this measurement, an estimate for the sensitivity to trapped flux S yields up to $(2.2 \pm 0.2)n\Omega/\mu T$.

4.2.3. Flux-dynamics during phase transitions. Calibrated magnetic sensors (AMR sensors) attached to the cavity can be used to measure the amount of trapped flux $\Delta B = B_{sc} - B_{nc}$ during cooldown and warm up. This measurement is shown
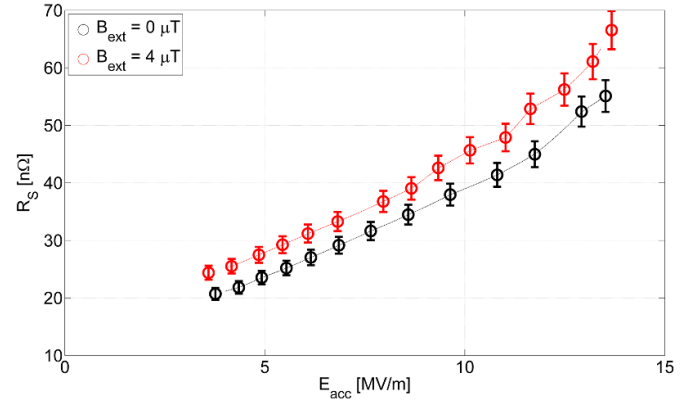

Figure 12. Surface resistance R_S versus accelerating field E_{acc} of 1DE16 taken at 16 mbar (1.8 k) at HZB. The ambient magnetic field during cooldown was either 4 μT (red) or canceled with the Helmholtz-coils (black). The bars give the 95% confidence level.
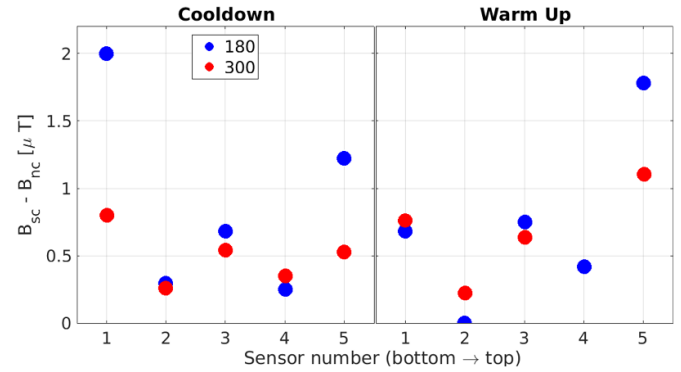

Figure 13. Difference of AMR sensor read outs before/after crossing T_c of the two H-mapping cards at 180° and 300°, the sensors are arranged from bottom (No. 1) to top (No. 5). The left plot shows the ΔB value during the cooldown, the right plot the ΔB value during the warm up. (The AMR sensor No. 4 at 300° failed prior to warm up). The relative error for the measurement is less then 2.5% [33].

in figure 13. The comparison of the ΔB values for cooldown and warm up is shown in figure 14. The measurement showed that the AMR sensors at the top of the cavity cell registered a slight increase of $\Delta B = 0.5\mu T$. A more severe change of $\Delta B = 1.4\mu T$ at 180° at the bottom of the cavity cell was observed. This position on the cavity surface is in agreement with the quench spot of the reference measurement displayed in figure 9. A possible cause for this different ΔB value during warm up compared to the cooldown could be a significant amount of flux entering the cavity during the test. This observation, together with an increase of the surface resistance difference above 9 MV m^{-1} as shown in figure 12 fit well with the model that flux lines enter at that accelerating field which then creates additional losses.

4.3. Heating of inner cavity surface

An estimate of the inner cavity temperature is possible assuming homogenous joule heating without any interface resistance. The surface resistance R_s for a given applied external
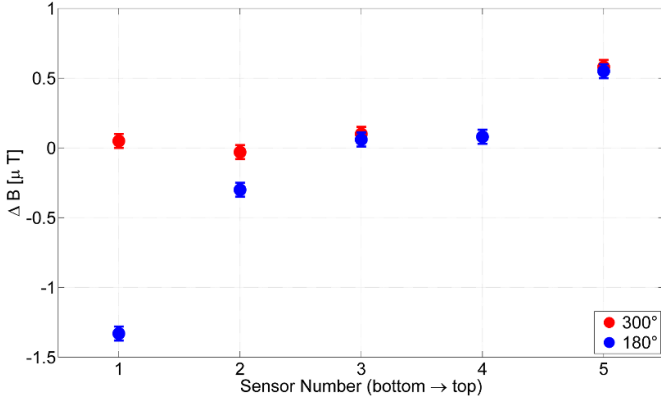
Figure 14. The difference in the ΔB values observed between cooldown and warm up for the different sensors from figure 13. A large difference at the bottom sensor No. 1 around 180° of about 1.4 µT is observed. The bars give the 95% confidence level.

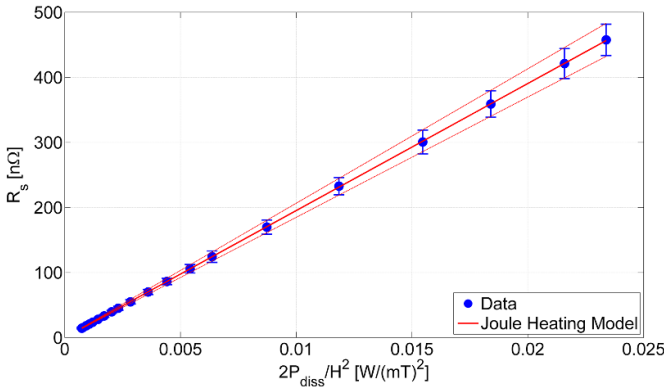**Figure 15.** Surface Resistance R_s vs. $2P_{diss}/H^2$ for 1DE16. Assuming homogenous joule heating, an area A_{fit} of (509.2 ± 0.6)cm^2 is derived as best fit. The bars give the 95% confidence level.

magnetic field H can be calculated via:

$$R_s = \frac{2P_{diss}}{AH^2} \quad (5)$$

with P_{diss} as the dissipated power of the cavity, obtained from the rf measurement and A as the effective area of heating. Figure 15 shows the experimental data together with the best fit. Assuming homogenous heating and an area A_{fit} of 509.2 ± 0.6 cm^2, a good agreement between the data and the model is found. The derived area A_{fit} can be projected onto the cavity surface where the equator is placed in the center of the projection since the highest magnetic field, and hence highest joule heating, is in this region. The area then has a width of equator ± 39 mm. Comparing this projected area with figures 11 or 16 shows that the region covers the *y*-axis from sensors 6 to 15, including major parts of the cell and all hot spots.

The thermal conductance through a planar, two-layered wall can be calculated via

$$\dot{Q} = P_{diss} = \frac{A_{fit} \cdot (T_{inside} - T_{outside})}{\frac{d_{Nb}}{\kappa_{Nb}} + \frac{d_{dirty}}{\kappa_{dirty}}} \quad (6)$$

with the derived area A_{fit}, the temperature of the inner cavity surface T_{inside}, the temperature of the outer cavity surface $T_{outside}$ obtained with the temperature mapping, the dissipated power P_{diss} measured during the rf test, the thermal conductivity κ_i and thickness d_i of the respective layers. The thermal conductivity of RRR 300 niobium at 1.8 K can be taken from literature, e.g. [34], and we will use 9 W mK^{-1}. The thickness of the layer is the wall thickness of the cavity, 2.8 mm, minus the thickness of the polluted layer. For the thickness of the polluted layer, only lower limits can be directly obtained from our measurements, e.g. the f vs. T data set or the later SIMS measurements. But assuming that carbon is the main pollution originating from the 800 °C step, the diffusion length can be calculated as the upper limit of the layer thickness. Taken the values for the activation energy E_a and the diffusion constant D_0 for carbon from [35], the diffusion length of 51.4 μm at 800 °C and for 3 h is derived, which will be used as layer thickness of the dirty layer. To estimate the thermal conductivity of the dirty layer, only reasonable estimates can be made. The thermal conductivity of Nb$_2$C and NbC at 1.8 K shows a significant spread depending on the actual stoichiometry [36] and an average of 0.3 W mK^{-1} will be used. Another possible estimation can be given by the RRR of the dirty layer obtained from the f vs. T measurement. Given an heuristic equation from [34], the thermal conductivity at 4.2 K can be derived by RRR/4 in [W mK^{-1}], which here yields to 1.25 W mK^{-1}. This is only an upper limit, since the thermal conductivity will decrease with decreasing temperature, but further justifies the assumed value of 0.3 W mK^{-1} at 1.8 k.

Using the estimated thicknesses and thermal conductivities of these two layers and neglecting any interface resistance in this calculation, a value of the inner cavity surface temperature T_{inside} of 2 K is derived which shows a significant heating. Using this obtained temperature and all obtained material parameters and exact cavity frequency, the total surface resistance R_s can be calculated to be on the order of 16 nΩ, while the measured total surface resistance R_s is 60 nΩ. From this rough estimation it is obvious that a heating because of the polluted layer indeed takes place, but this temperature increase is not enough to explain the observed drastic deterioration of the quality factor.

5. Cut-out studies

The guiding questions for the extensive cut-out analysis program were:

(a) Are niobium carbides forming on the inner cavity surface?
(b) Are niobium carbides related to the cavity rf deterioration?
(c) Why do we observe niobium carbides on all samples while the cavity performance shows a considerable spread?

Hence, regions of interest were identified and surface analysis methods where then tailored according to the questions.
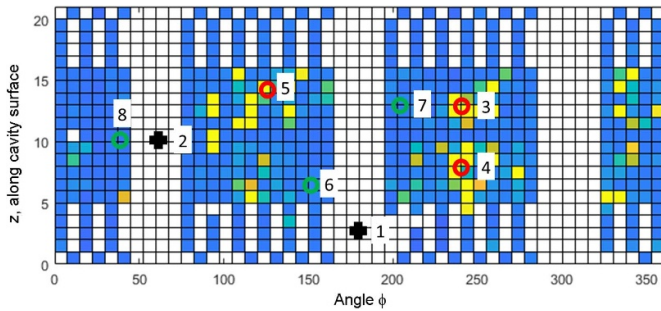
Figure 16. Temperature map of 1DE16 taken at 1.5 K at HZB. White areas are the position of the H-Map cards. Markers for the samples cut from quench spots (black), hot spots (red) and cold spots (green) are shown.

5.1. Cavity dissection

To further identify regions of interest, the temperature map of 1DE16 was also taken at 1.5 K to emphasize the residual resistance contribution and to better identify local hot or cold spots, see figure 16. All regions of interest are marked, together with the number of the sample cut from it. Furthermore, an optical inspection system at DESY was used to look for regions of interest on the inner cavity surface [37, 38], but no defect or impurity was observed. A list of samples containing their original positions with respect to the cavity coordinate system and the respective method used to identify the associated region is given in table 2. Prior to cutting the samples from 1DE16, a test of the cutting tool (*Fein Multimaster*) was done on a dummy cavity. The sample surface was observed with an optical pyrometer during the process and a heating up to 80 °C was observed. Hence for 1DE16, the sample area was cooled with pressurized air, aimed at the outer surface, while cutting the square-shaped samples. The observed surface temperature never rose above 40 °C. The samples have an edge length of ≈ 15 mm, which translates to roughly two squares in the z- and one square in the ϕ-direction at the equator and up to three squares in the ϕ-direction closer to the beam pipe looking at the temperature map in figure 16.

5.2. Are niobium carbides forming on the inner cavity surface?

The scanning electron microscope (SEM) at the DESY Nano-Lab [39] was used to investigate all of the samples cut from the cavity. From all samples, a series of images was taken with the same parameters with respect to the applied voltage and magnification, to have a comparable set between the samples. One such image is shown in figure 17. In addition, EDX was performed. A high amount of carbon was observed in all spectra, regardless of the position on the sample. However, the carbon signal was larger in precipitates compared to the background, leading to the conclusion that carbon enriched precipitates were formed on all samples. Further x-ray photoelectron spectroscopy (XPS) measurements confirmed the existence of the Nb_2C phase.
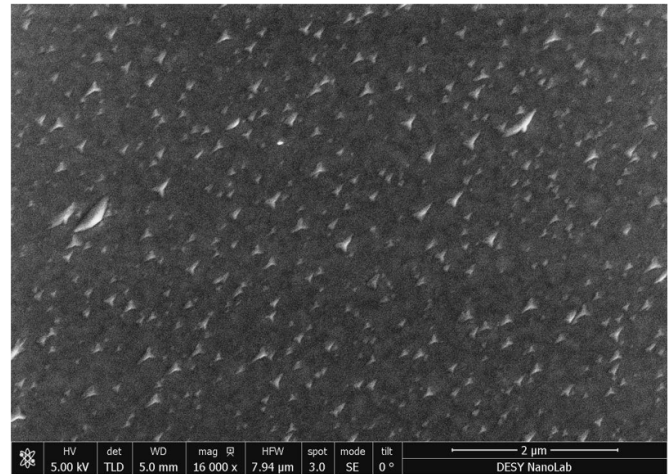

Figure 17. SEM image of sample 2. Star-shaped precipitates are observed on all samples.
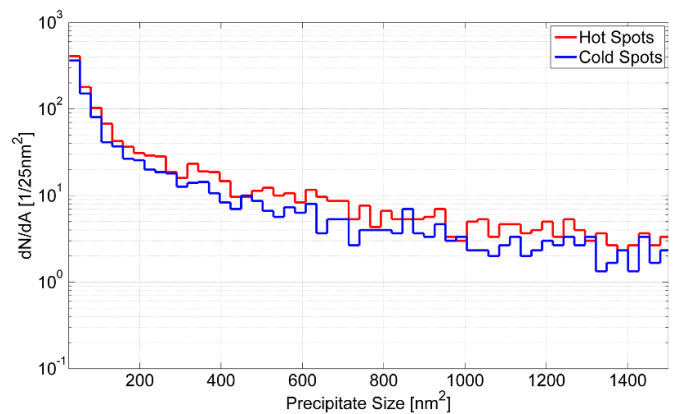

Figure 18. The plot shows the size distribution of the niobium carbides averaged for hot spots (red) and cold spots (blue). The total amount of observed carbides is less in cold spots than in hot spots.
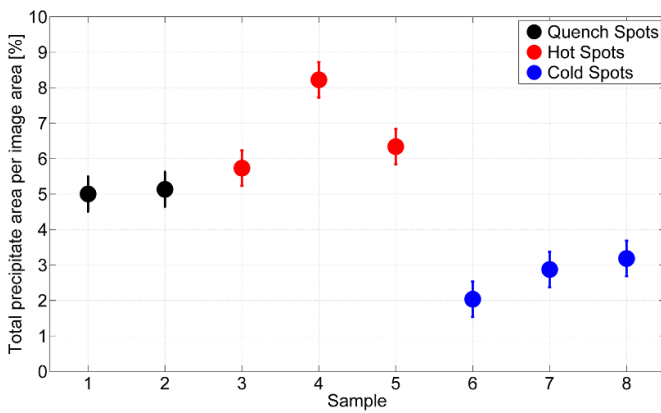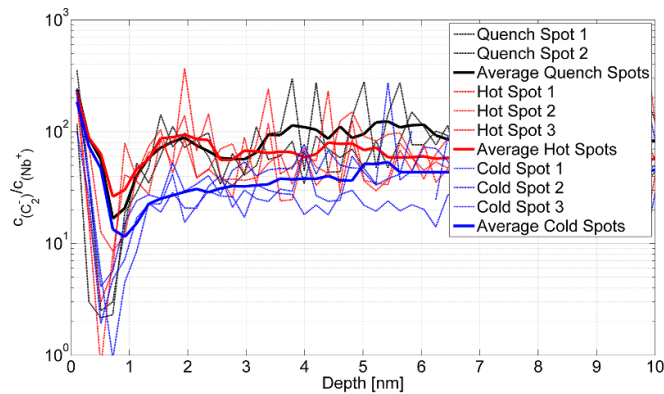
5.3. Are niobium carbides related to the cavity rf deterioration?

5.3.1. Surface analysis.
The size and amount of the precipitates observed with the SEM were measured with an efficient object detection algorithm [37] in Matlab™. The averages of the size distributions for the hot spot samples 3-5 compared to the cold spot samples 6-8 are shown in figure 18. More and larger precipitates were found on hot spot samples compared to cold spot samples. The fraction of the image area covered by precipitates is shown in figure 19. Consequently, a larger area per image was covered with precipitates for quench spots and hot spots compared to the cold spots. In addition, XPS measurements of the samples showed that the signal for the niobium-carbide phase was the strongest for the sample 2 which was the quench spot after the infusion run.

5.3.2. Depth profiling.
As a next step, ToF-SIMS was applied, in order to investigate the depth profile of the elements bound to or interstitial in the niobium. The sputter parameter were 3 keV Argon ions on a surface of 300×300 μm^2 with

Table 2. List of cut-outs of 1DE16, their positions and type.

Sample	Position Angle ϕ	Height z	Diagnostic	Type
	170°	Below equation	T-Map DESY	
1	170°	equation− 24 mm	Second Sound 1st run	Quench
	170°	near beam pipe	H-Map HZB	
2	70°	on equation	Second Sound 2nd run	Quench
3	240°	equation+20 mm	T-Map HZB	Hot Spot
4	240°	equation−10 mm	T-Map HZB	Hot Spot
5	115°	equation+15 mm	T-Map HZB	Hot Spot
6	115°	equation−10 mm	T-Map HZB	Cold Spot
7	215°	equation+10 mm	T-Map HZB	Cold Spot
8	30°	on equation	T-Map HZB	Cold Spot

Figure 19. The total area of observed carbides per image area for quench spots (black), hot spots (red) and cold spots (blue). The bars give the 95% confidence level.

Figure 20. Normalized C_2^--signal of each sample in the first 10 nm obtained with a ToF-SIMS. Quench spots and hot spots showed a higher carbon content in this layer.

analysis parameters of 25 keV Bismuth ions on a surface of 102×102 μm^2 in the center of the sputter crater. No nitrogen signal was observed in any of the samples and no systematic differences for any element except carbon was found between the samples. Figure 20 shows the carbon concentration signal normalized to the niobium signal of the samples. In agreement

with the SEM image analysis, a higher carbon concentration was detected in the hot spots and quench spots compared to the cold spots.

5.4. Origin of uneven carbon aggregation across samples?

Facing the fact that we observe niobium carbides on all samples cut from the same cavity, but the size and density distribution as well as the carbon content varies between the samples, the question arose what is the origin of the varying carbon aggregation.

5.4.1. Crystal orientation. The crystal structure was mapped utilizing electron backscatter diffraction (EBSD) which gathers data from the first 100 nm. On each sample, two different spots were scanned with an 220×160 grid and a 10 μm step size. On average, 619 ± 115 grains per sample were scanned (not including grains at the boundary of the grid), while the two samples from the equatorial weld (2 and 8) only showed 31 grains. An example image of the obtained grain orientation is given in figure 21. The grain orientation distributions projected on inverse pole figures for all hot spots and cold spots are shown in figure 22. While the dominant grain orientation in all samples is the [001] direction, for hot spots significant contributions of the grain orientations along the [112] and [113] direction is observed.

To study low-angle grain boundaries, the *local misorientation* can be used. It is defined as the average angle between a center point and its set of nearest neighbors, where only angles below a threshold angle Θ contribute to exclude large-angle grain boundaries [40, 41]. Creating a map of these angles allows us to visualize the lattice defects, such as dislocations, within grains. This provides a measure of the recrystallization rate of the material. In this case, the threshold angle Θ was 2.5° and a 3×3 neighborhood was used. Analyzing the local misorientation of the crystal lattice obtained during this measurement resulted in the distributions of the low-angle grain boundaries shown in figure 23. A distinct difference between hot spots and cold spots is observed. The two quench spots sample 1 and 2 showed narrow distributions of low-angle grain
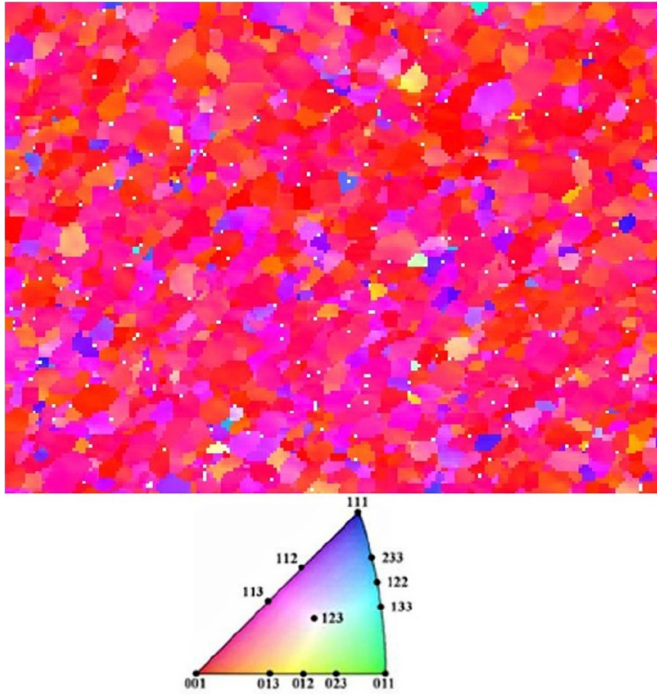
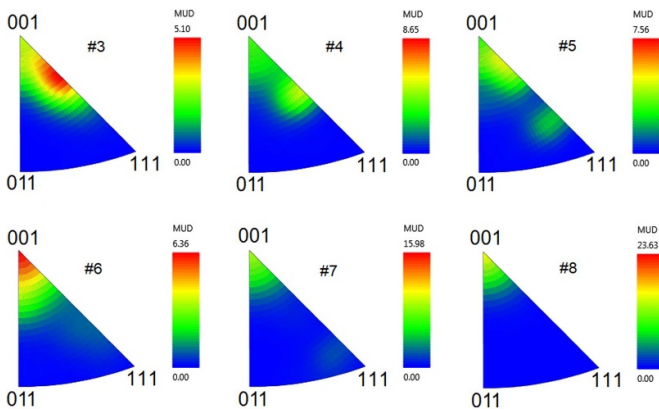**Figure 21.** The grain orientation for hot spot sample 3 is shown.

Figure 22. Inverse pole figures showing the grain orientations with respect to the surface normal of the three hot spot samples 3–6 (top) and three cold spot samples 4–8 (bottom). Colors indicate multiples of uniform distribution (MUD).

boundaries with peaks at $0.17 \pm 0.02\%$. The local misorientation map of sample 1 showed no intra-grain boundaries but a rather homogenous, small local misorientation density, offering no explanation why this region was a quench spot and showed such a strong flux trapping. Sample 2 was cut from the equatorial weld region, which underwent recrystallization and grain growth during the weld. Hence, a distinct difference in the crystal structure was expected compared to samples from the rest of the surface. Still, the observed properties with EBSD do not indicate any explanation for the quench. A thorough study on the grain boundaries is planned next.

5.4.2. Vacancy Concentration. To further investigate the crystal lattice structure, positron annihilation lifetime
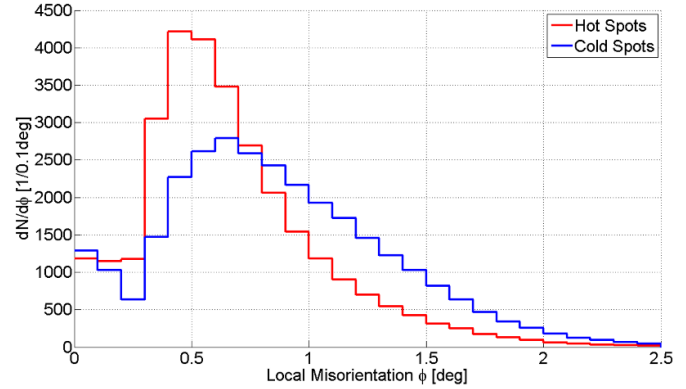

Figure 23. Averaged local misorientation distribution for hot spots (red) and cold spots (blue).

spectroscopy (PALS) was applied to the samples which is used to measure the vacancy type and concentration as a function of positron implantation depth. As positrons can easily get trapped in metal vacancy defects and are known to be very sensitive to their chemical environment, they are the optimal choice to analyze the types, concentrations and atomic environment of vacancies [42]. The spot size diameter of the positron beam was of the order of 10 mm. The measurements showed three contribution to the lifetimes attributed to two different types of defect: (i) a short-lived component with lifetime τ_1 and intensity I_1 representing a contribution of free positrons delocalized in the lattice (not trapped at defects). (ii) a medium-lived component with lifetime τ_2 and intensity I_2 which can be attributed with positrons trapped at vacancy-hydrogen complexes [42, 43]. (iii) a long-lived component with lifetime τ_3 and intensity I_3 which can be attributed to positrons trapped at larger defects, e.g. vacancy clusters, and positrons annihilated in the surface state. The mean lifetime $\tau_{\mathrm{mean}} = I_1\tau_1 + I_2\tau_2 + I_3\tau_3$ for the samples are shown in figure 24. The measurements showed a systematic difference between the hot spot or cold spot samples observable in the mean lifetime. Cold spot samples exhibit a slightly higher value, especially above 3 keV. The major effect for this difference is the lifetime for long-lived component, which is larger for the cold spots compared to the hot spots. Another additional deviation was found for the quench spot before the failed infusion: Sample 1 has a significantly larger mean positron lifetimes between 24 keV which translates to the first 60 nm. This is due to an increased positron lifetime τ_3 and intensity I_3, while the intensities from the other contributions are lower compared to the other samples. Hence, sample 1 contains more and significant larger vacancy clusters within the rf penetration layer compared to the other samples.

5.4.3. Elemental analysis. Motivated by the findings in [15], in which a titanium contamination in the furnace lead to a deterioration similar to the one observed in our case, a dedicated analysis to identify such a possible contamination was done. In [44], proton-induced x-ray emission (PIXE) was used to analyze titanium in niobium cavities, since this method has a better sensitivity for heavier elements than other x-ray induced
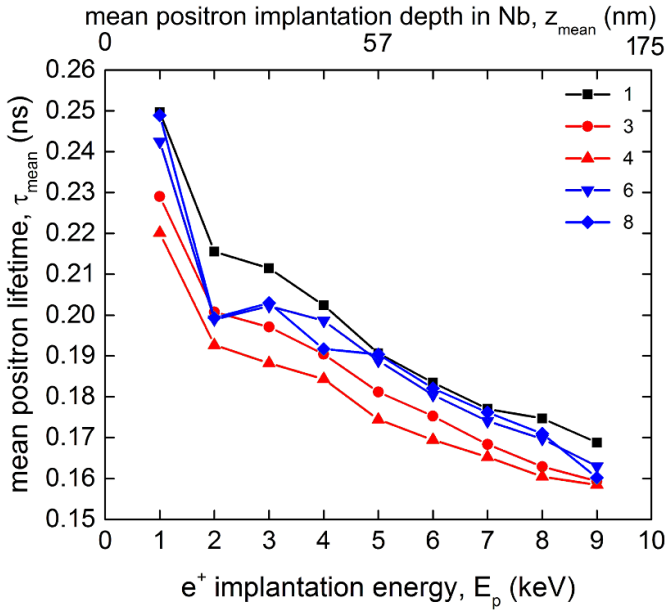
Figure 24. Mean positron lifetime, measured at room temperature, versus the positron implantation depth for the indicated samples.
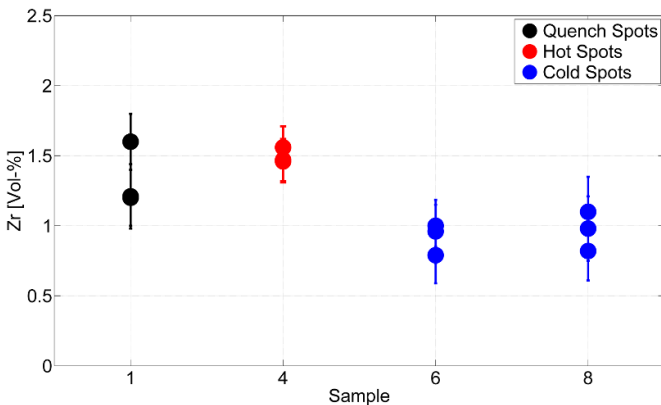

Figure 25. Zirconium concentration for four samples according to PIXE. A slightly higher concentration in the hot spot and quench spot samples compared to the cold spots samples was found. The bars give the 95% confidence level.

measurements. The measurement was done on four of the eight samples, namely the quench spot sample 1, hot spot sample 2 and the cold spot samples 6 and 8. Each sample was analyzed on three different spots, each spot with an area of 1 mm, and a total depth of 10 μm. One additional spot per sample was on the cutting surface to cross-check obtained surface results. No titanium signal was observed. On the other hand, a relevant signal from zirconium was found in the samples - the result is shown in figure 25.

A slightly higher concentration in the hot spot and quench spot samples were found than in the cold spot samples. Although uncommon, zirconium is a known impurity in niobium [45]. On several cutting surfaces but not on the sample surfaces, additional strong signals on the order of 100-1000 ppm of Fe, Cr and Co were found, which fit the composition of the cutting tool used. Since the zirconium signal was found on the cutting surface and on the sample surface, it is more likely that it is a real interstitial signal and not another contamination from the cutting tool.

6. Summary and conclusion

The nitrogen infusion R&D at DESY is ongoing after facing several performance issues in the beginning. The very first infusion runs resulted in a severe deterioration of the cavities. To study the degradation, one cavity was extensively characterized and samples were cut from it and analyzed.

The three main questions guiding the study were whether niobium carbides formed on the inner cavity surfaces during the infusion runs at the DESY furnace; how the hypothetical carbides relate to the rf performance; and why similar infusion processes resulted in a considerable spread in the rf performance of the cavities.

In section 5.2 we demonstrated that the carbides indeed form on the inner cavity surface leading us to the second question if the carbides cause the deterioration. The data provided in figure 19 indicates that there is a relation between the area/volume covered by niobium carbides and the local heating. In agreement to that, the carbon concentration in cold spots was lower compared to hot spots and quench spots according to figure 20. These results suggest that niobium carbides are the cause for the deterioration.

We then started to investigate the underlying type of the deterioration. The value for the sensitivity to trapped flux S is remarkably small and close to that of a standard treated cavity [31, 32, 46] and only the quench spot prior to the treatment exhibited significant flux trapping behavior with an higher η. Niobium cavities with such a small mean free path as measured for this cavity are usually regarded as highly susceptible to trapped flux [47, 48]. Nevertheless, recent calculations and observations showed that a small sensitivity value can be in agreement with a large density of pinning sites, equivalent to a small mean free path [31, 32, 49]. Hence, this observed sensitivity does not disagree with the assumption of the formation of niobium carbides on the surface causing the observed small mean free path ℓ. Based on this measurement, we conclude that trapped flux contributed little to the increased losses.

As a next step, we investigated the impact of thermal feedback. The thermal conductivity of niobium carbides is smaller than that of niobium [36] and in [50] it was argued that an increase of interstitial carbon in niobium can lead to a decrease of T_c, hence increasing the surface resistance. The small surface resistance at low accelerating fields is in agreement with this model, since Nb_2C has a T_c of 1.98 K [51] and can be superconducting by proximity effect below a certain breakdown field [52]. This is similar to the well known Q-Disease caused by niobium hydrides [53, 54].

The observed decrease of the reduced gap value $\Delta/k_B T_c$ from 1.97 to 1.79 for 1DE18 fits as well with the thermal feedback model in [55–57] since a reduction of the gap value yields to a reduced onset field of the Q-drop as observed here. Nevertheless, the calculations in section 4.3 showed that

although a significant heating of 0.2 K was derived and a higher than normal surface resistance R_s at 1.8 K, with this simple model the high surface resistance could not be fully explained. Hence, we conclude that a thermal feedback model might play a role but is not the leading cause for the observed deterioration.

Following the results of titanium contamination of cavities due to a titanium pollution in the furnace which lead to the same shape of the Q_0 vs. E_{acc} curves [15], an search for titanium was done but none was found in any sample. As has been shown in [58], it is actually the loading of grain boundaries with titanium causing the deterioration and in [59], NbTiN films on a Nb cavity showed the same Q_0 vs. E_{acc} curves. For the latter case, the high granularity of the films were believed to cause the losses. Grain boundaries form weak Josephson junctions which a superconducting current has to pass. If the current density surpasses the critical current density of the Josephson junctions, the grains will decouple acting as an array of individual resistors [59–61]. Loading grain boundaries with interstitials, such as titanium or as in this case carbon, can reduce the critical current density [62] and hence, the decoupling occurs at magnetic field values below that of pure niobium. Further supporting this possible explanation, the same decay constant as in [58] has been derived for 1DE16 and 1DE17 with $(0.14 \pm 0.01)1/MV/m$.

Finally, the question remained why cavities exhibited only limited change in rf performance after infusion runs while witness samples still showed a significant amount of precipitates. In section 5.4, the characterization of the cut-outs in terms of crystal structure and heavy elements are discussed and measurements showed distinct differences in properties such as vacancy types and densities, crystal orientations, low-angle grain boundaries and interstitials between the hot spots and cold spots.

As has been shown in [50], Nb_2C is the most stable phase for carbon in Nb, but accumulations of carbon near vacancies can form C-C dimer and carbon-vacancy complexes, which are kinetically competitive to NbC. Hence, a higher vacancy concentration in the cold spots, as found with PALS, might statistically suppress the formation of Nb_2C, explaining the lower Nb_2C-density found on cold spots. Furthermore, [36] demonstrated that the thermal conductivity below 20 K of niobium carbides is further decreased for crystals with lower vacancy concentrations. In the present samples, PALS measurements, shown in figure 24, revealed that the intensity of the third positron lifetime contribution I_3, proportional to the vacancy concentration, in the hot spot samples were lower than for cold spot samples, leading to an additional increase in dissipation.

In [63, 64] it was observed that grain boundaries have a significant influence on the carbon diffusion in niobium, and in general in bcc lattices, and that the actual grain boundary orientation determines whether the diffusion along the grain boundary is enhanced, suppressed or if the grain boundary act as trapping potential for carbon [65]. Low-angle grain boundaries within a grain compensate exactly the small misorientation needed to turn an arbitrary grain boundary to the nearest orientation with lower energy and superimpose it on this very boundary. And studies in ferrite systems showed that the misorientation angle for low-angle grain boundaries and the grain boundary plane and rotation axis for high-angle grain boundaries have a significant influence of the carbon segregation along the grain boundaries [66] and in [67], the penetration along grain boundaries as a function of the grain boundary angle for bcc lattices showed a maximum for a certain angular range and suppressed penetration for other. A distinct difference between hot spots and cold spots regarding the low-angle grain boundaries was observed, see section 5.4.1, hinting at another fundamental difference in the local crystal topography and the importance of the grain boundaries and a more detailed study on the grain boundary orientations is ongoing.

Furthermore, the dominant grain orientation within cold spots spots was [001] while additional contributions from the [112] orientation was observed for hot spots. The {112} plane is a slip plane for niobium. It is known that dislocation diffusion along slip planes is enhanced, which can explain the difference of the low-angle grain boundaries within the lattice near the surface observed in figure 23. In addition, carbon diffusion along slip planes and dislocation cores in bcc lattices seems to be suppressed [68].

To summarize, the overall lattice structure differs significantly between hot spots and cold spots, causing several effects of carbon dynamics and interactions of varying impact. In addition, interstitial zirconium, as found with PIXE (see figure 25), can act as a catalyst in niobium-carbon reactions [69], fostering the formation of more stable zirconium-enriched (Nb,Zr)-C complexes.

The absence of nitrogen in any sample and no improvement of any cavity which underwent infusion with nitrogen can also be explained by the increased carbon concentration. Interstitial carbon and nitrogen atoms both prefer the octahedral position in the bcc lattice of niobium, while carbon has an energetically favorable binding energy compared to nitrogen [50]. Hence, if the carbon enters the niobium during the 800 °C phase, a later injection of nitrogen into the furnace during the 120 °C phase can be completely ineffective. The niobium surface might not be clean enough and the lattice saturated with carbon hence suppressing or preventing the nitrogen adsorption and diffusion into the niobium.

We conclude that witness samples allow to assess the quality of the furnace and to understand the processes taking place on the niobium surface but have only limited ability to predict the rf performance of the cavities after the respective furnace run. Additional information on the crystal structure of the cavity must be taken into account.

The origin of the carbon pollution has been traced back to the furnace vacuum itself. A high CO and CO_2 contribution observed in the RGAs is evident as shown in figure 6, and an inverse correlation between the quality factor at 4 MV m^{-1} and the total pressure at 800 °C is observed, see section 3.2.2. In agreement to that, the formation of star-shaped Nb_2C precipitates on niobium samples annealed at 700 to 1200 °C for 40 min in a partial pressure for CO and CO_2 of 1.3×10^{-6} mbar while undergoing H$^+$ irradiation was already reported in [70]. There, the adsorption and diffusion of the carbon from the residual gas into the niobium was identified as the origin of the formation the niobium

carbides. Hence, the observed correlation between the quality factor and the total pressure might actually be a correlation with the partial pressure of CO and CO_2. Thus, an improvement on the vacuum system of the furnace is currently being prepared.

The issues with transferring a nitrogen treatment recipe from one furnace to another however remains. It is clear that the specified nitrogen infusion recipe does not contain all relevant information and key parameters, e.g. limits on the partial pressures of the furnace, relevance and preparation of niobium caps, and that further R&D is necessary to reach a stable, repeatable and transferable recipe.

As an interesting additional result, a most likely microscopic cause of the quench before the infusion, hence before the formation of niobium carbides, was found. The quench spot before the infusion at $170°$ close to the bottom beam pipe showed a significant amount of flux trapping during rf test with no heating prior to the quench (see section 4.1 and 4.2). The sample from this region showed a significant larger mean positron lifetime, see figure 24, originating from more and larger vacancy-clusters within the first 60 nm compared to the other samples. The negative effect of lattice defects such as near-surface vacancy-clusters on the *field of first flux penetration* is generally known [71]. Hence, the most reasonable explanation for the magnetic quench are vacancy-clusters allowing magnetic flux lines to enter the cavity during the rf test.

Acknowledgment

ORCID iDs

Marc Wenskat https://orcid.org/0000-0001-6546-770X
Thomas F Keller https://orcid.org/0000-0002-3770-6344
Lea Steder https://orcid.org/0000-0001-9844-1119

References

[1] Brinkmann R, Schneidmiller E A, Sekutowicz J and Yurkov M V 2014 Prospects for CW and LP operation of the European XFEL in hard X-ray regime *Nucl. Instrum. Methods Phys. Res.* A **768** 20–5

[2] Wenskat M *et al* 2018 Nitrogen infusion R&D for CW operation at DESY *Proc. of LINAC2018* pp 652–7

[3] Grassellino A *et al* 2017 Unprecedented quality factors at accelerating gradients up to 45MV/m in niobium superconducting resonators via low temperature nitrogen infusion *Supercond. Sci. Technol.* **30** 094004

[4] Dhakal P, Chetri S, Balachandran S, Lee P J and Ciovati G 2018 Effect of low temperature baking in nitrogen on the performance of a niobium superconducting radio frequency cavity *Phys. Rev. Accel. Beams* **21** 032001

[5] Grassellino A *et al* 2013 Nitrogen and argon doping of niobium for superconducting radio frequency cavities: a pathway to highly efficient accelerating structures *Supercond. Sci. Technol.* **26** 102001

[6] Koufalis P N, Hall D L, Liepe M and Maniscalco J T 2016 Effects of interstitial oxygen and carbon on niobium superconducting radio-frequency resonators arXiv:1612.08291

[7] Maniscalco J T, Gonnella D, Liepe M and Gonnella D 2017 The importance of the electron mean free path for superconducting radio-frequency cavities *J. Appl. Phys.* **1211** 213903–23908

[8] Umemori K 2020 New results of KEK infusion and mid-T bake *Proc. of TTC 2020* Geneva

[9] Longuevergne D 2020 Status of infusion studies at IJClab/CEA-saclay *Proc. of TTC 2020* Geneva

[10] Gurevich A and Kubo T 2017 Surface impedance and optimum surface resistance of a superconductor with an imperfect surface *Phys. Rev.* B **96** 184515

[11] Checchin M, Martinello M, Melnychuk O S, Sergatskov D A, Posen S, Grassellino A and Romanenko A 2018 New insight on nitrogen infusion revealed by successive nanometric material removal *Proc. of IPAC2018* Vancouver

[12] Kubo T and Gurevich A 2019 Field-dependent nonlinear surface resistance and its optimization by surface nano-structuring in superconductors arXiv:1907.12040v1

[13] Maniscalco J T, Ge M, Koufalis P N, Liepe M, Arias T A, Liarte D B, Sethna J P and Sitaraman N 2019 The field-dependent surface resistnace of doped niobium: new experimental and theoretical results *Proc. of SRF2019* Dresden

[14] Trenikhina Y, Grassellino A, Melnychik O and Romanenko A 2015 Characterization of nitrogen doping recipes for the Nb SRF cavities *Proc. of SRF2015* pp 223–7

[15] Grassellino A *et al* 2013 Fermilab experience of post-annealing losses in SRF niobium cavities due to furnace contamination and the ways to its mitigation: a pathway to processing simplification and quality factor improvement arXiv:1305.2182

[16] Reschke D, Gubarev V, Schaffran J, Steder L, Walker N, Wenskat M and Monaco L 2017 Performance in the vertical test of the 832 nine-cell 1.3 GHz cavities for the European X-ray Free Electron Laser *Phys. Rev. Spec. Top. Accel. Beams* **20** 042004

[17] Aderhold S, Chel S, Elsen E, Eozénou F, Lilje L and Reschke D 2010 Cavity process *Tech. Rep.* (DESY, Hamburg)

[18] Aune B *et al* 2000 Superconducting TESLA cavities *Phys. Rev. Spec. Top. Accel. Beams* **3** 21–45

[19] Barzilai S, Raveh A and Frage N 2005 Annealing of niobium coatings deposited on graphite *Vacuum* **79** 171–7

[20] Barzilai S, Frage N and Raveh A 2006 Niobium layers on graphite: Growth parameters and thermal annealing effects *Surf. Coat. Technol.* **200** 4646–53

[21] Bate C *et al* 2019 Nitrogen Infusion Sample R & D at DESY *Proc. of SRF2019*

[22] Pekeler M *et al* 1996 Thermometric study of electron emission in a 1.3 GHz superconducting cavity *Particle Accelerators* **53** 35–52

[23] Tamashevich Y 2017 Diagnostics and treatment of 1.3 GHz Nb cavities Ph.D. thesis Hamburg

[24] Bosse B 2019 Systematische studien eines systems zur lokalisierung von cavity quenches Master thesis Hamburg

[25] Maier L C and Slater J C 1952 Field Strength Measurements in Resonant Cavities *J. Appl. Phys.* **23** 68

[26] Gorter C and Casimir H 1934 Zur thermodynamik des supraleitenden zustandes *Z. Tech. Phys.* **15** 539–42

[27] Pippard A and Bragg W L 1953 An experimental and theoretical study of the relation between magnetic field and current in a superconductor *Proc. R. Soc.* A **216** 547-68

[28] Turneaure J P, Halbritter J and Schwettman H A 1991 The surface impedance of superconductors and normal conductors: The Mattis-Bardeen theory *J. Supercond.* **4** 341–55

[29] Bonin B 1995 *Materials for superconducting cavities Tech. Rep. 2* CERN

[30] Schmitz B, Köszegi J, Alomari K, Kugeler O and Knobloch J 2018 Magnetometric mapping of superconducting RF cavities *Rev. Sci. Instrum.* **89** 54706

[31] Dhakal P, Ciovati G and Gurevich A 2019 Flux expulsion in niobium superconducting radio-frequency cavities of different purity and essential contributions to the flux sensitivity arXiv:1906.04163

[32] Dhakal P, Ciovati G and Gurevich A 2020 Flux expulsion in niobium superconducting radio-frequency cavities of different purity and essential contributions to the flux sensitivity *Phys. Rev. Accel. Beams* **23** 023102

[33] Ueki R, Okada T, Masuzawa M, Tsuchiya K, Kawamoto T, Umemori K, Kako E, Konomi T and Sakai H 2020 Study on Magneto-Resistance Sensors for Low Magnetic Field Measurements *IEEE Trans. Appl. Supercond.* **30** 30

[34] Koechlin F and Bonin B 1996 Parametrization of the Niobium Thermal Conductivity in the Superconducting State *Supercond. Sci. Technol.* **9** 453

[35] Fromm E and Gebhardt E 1976 *Gase und Kohlenstoff in Metallen. Reine und Angewandte Metallkunde in Einzeldarstellungen* (Berlin-Heidelberg-New York: Springer) p 747

[36] Jasperson S X, Schxatterly A S E, Radosevicht L G, O'endell A and Williams S 1969 Lattice thermal conductivity of superconducting niobium carbide *Phys. Rev.* **188** 770–3

[37] Wenskat M 2017a Automated optical inspection and image analysis of superconducting radio-frequency cavities *J. Instrum.* **12** 05016

[38] Wenskat M 2017b Optical surface properties and their RF Limitations of European XFEL Cavities *Supercond. Sci. Technol.* **30** 105007

[39] Stierle A, Röhlsberger R, Noei H, Keller T F and Vonk V 2016 DESY NanoLab *J. Large-Scale Res. Facil.* **A76** 1–9

[40] Wright S I, Nowell M M and Field D P 2011 A Review of Strain Analysis Using Electron Backscatter Diffraction *Microsc. Microanal.* **17** 316–29

[41] Wright S I, Nowell M M, De Kloe R and Chan L 2014 Orientation Precision of Electron Backscatter Diffraction Measurements Near Grain Boundaries *Microsc. Microanal.* **20** 852–63

[42] Cizek J 2018 Characterization of lattice defects in metallic materials by positron annihilation spectroscopy: A review *J. Mater. Sci. Technol.* **34** 577–98

[43] Visentin B, Barthe M F, Moineau V and Desgardin P 2010 Involvement of hydrogen-vacancy complexes in the baking effect of niobium cavities *Phys. Rev. Spec. Top. Accel. Beams* **13** 052002

[44] Antoine C, Bonin B, Safa H, Berthier B, Tessier C, Tocellier P, Chevarier A, Chevarier N and Roux B 1997a Evidence of preferential diffusion of impurities along grain boundaries in very pure niobium used for radio frequency cavities *J. Appl. Phys.* **81** 1677

[45] Singer W, Singer X, Brinkmann A, Iversen J, Matheisen A, Navitski A, Tamashevich Y, Michelato P and Monaco L 2015 Superconducting cavity material for the European XFEL *Supercond. Sci. Technol.* **28** 085014

[46] Padamsee H, Knobloch J and Hays T 2008 *RF Superconductivity for Accelerators* (Weinheim: Wiley-VCH Verlag) p 521

[47] Gonnella D, Kaufman J, Koufalis P N and Liepe M 2016 RF losses from trapped flux in SRF cavities *Proc. of IPAC2016*

[48] Maniscalco J T, Gonnella D and Liepe M 2017 The Importance of the Electron Mean Free Path for Superconducting Radio-Frequency Cavities *J. Appl. Phys.* **121** 043910

[49] Martinello M, Grassellino A, Checchin M, Romanenko A, Melnychuk O, Sergatskov D A, Posen S, Zasadzinski J and Grassellino A 2016 Effect of interstitial impurities on the field dependent microwave surface resistance of niobium *Appl. Phys. Lett.* **109** 062601

[50] Ford D C, Zapol P and Cooley L D 2015 First-principles study of carbon and vacancy structures in niobium *J. Phys. Chem.* **119** 14728–36

[51] Kosolapova T Y 1971 *Carbides: Properties, Production and Applications* (New York: Plenum) p 310

[52] De Gennes P G and Hurault J P 1965 Proximity effects under magnetic fields. II - interpretation of 'breakdown' *Phys. Lett.* **17** 181–2

[53] Bonin B and Röth R 1992 Q degradation of niobium cavities due to hydrogen contamination *Proc. of SRF1991* vol 40 pp 59–83

[54] Antoine C and Berry S 2002 H in niobium: origin and method of detection *AIP Conf. Proc.* 13

[55] Ciovati G, Kneisel P and Gurevich A 2007 Measurement of the high-field Q drop in a high-purity large-grain niobium cavity for different oxidation processes *Phys. Rev. Spec. Top. Accel. Beams* **10** 1–19

[56] Ciovati G 2007 Review of high field Q slope, cavity measurements *Proc. of SRF2007* pp 70–4

[57] Gurevich A 2006 Multiscale mechanisms of SRF breakdown *Physica* C **441** 38–43

[58] Antoine C, Safa H, Berthier B, Galien J P, Chevarier A, Brossard F, Knobloch J and Padamsee H 1997 Nuclear microprobe studies of impurities segregation in niobium used for radiofrequency cavities *Proc. of SRF1997* pp 911–17

[59] Bonin B and Safa H 1981 Power dissipation at high fields in granular RF superconductivity *Supercond. Sci. Technol.* **4** 257–61

[60] Hylton T L, Kapitulnik A, Beasley M R, Carini J P, Drabeck L and Gruner G 1988 Weakly coupled grain model of high-frequency losses in high Tc superconducting thin films *Appl. Phys. Lett.* **53** 1343–5

[61] Halbritter J 1995 Granular superconductors and their intrinsic and extrinsic surface impedance Tech. Rep. 6

[62] Kasen M B 1970 Grain boundary resistivity of aluminium *Philos. Mag.*) **21** 599–610

[63] Bokstein B and Razumovskii I 2003 Grain boundary segregation and grain boundary diffusion of carbon in niobium. Comparison of data for substitution and interstitial solid solutions *Defect Diffus. Forum* **216-217** 123–32

[64] Kuan L *et al* 2018 Grain Boundary Plays a Key Role in Carbon Diffusion in Carbon Irons Revealed by a ReaxFF Study *J. Phys. Chem.* C **122** 23191–9

[65] Restrepo O A, Mousseau N, Trochet M, El-Mellouhi F, Bouhali O and Becquart C S 2018 Carbon diffusion paths and segregation at high-angle tilt grain boundaries in alpha-Fe studied by using a kinetic activation-relation technique *Phys. Rev.* B **97** 54309

[66] Herbig M, Raabe D, Li Y J, Choi P, Zaefferer S and Goto S 2013 Atomic-scale quantification of grain boundary segregation in nanocrystalline material *Phys. Rev. Lett.* **112** 1–5

[67] Haynes C W and Smoluchowski R 1955 Grain boundary diffusion in a body-centered cubic lattice *Acta Metall.* **3** 130–4

[68] Ishii A, Li J and Ogata S 2013 Conjugate channeling effect in dislocation core diffusion: carbon transport in dislocated BCC iron *PLoS One* **8** 60586

[69] Grobstein T L and Titran R H 1986 Characterization of precipitates in a niobium-zirconium-carbon alloy *Tech. Rep.* NASA/DOE

[70] Thomas G J and Bauer W 1975 Carbide formation on Nb surfaces during high-temperature H irradiation *J. Vac. Sci. Technol.* **12** 490–5

[71] Antoine C 2019 Influence of crystalline structure on rf dissipation in superconducting niobium *Phys. Rev. Accel. Beams* **22** 034801